

# Measuring irreversibility from learned representations of biological patterns

Junang Li,<sup>1,2,\*</sup> Chih-Wei Joshua Liu,<sup>1,\*</sup> Michal Szurek,<sup>1</sup> and Nikta Fakhri<sup>1,†</sup>

<sup>1</sup>*Department of Physics, Massachusetts Institute of Technology, Cambridge, MA 02139, USA*

<sup>2</sup>*Center for the Physics of Biological Function, Princeton, NJ, 08540, USA*

Thermodynamic irreversibility is a crucial property of living matter. Irreversible processes maintain spatiotemporally complex structures and functions characteristic of living systems. Robust and general quantification of irreversibility remains a challenging task due to nonlinearities and influences of many coupled degrees of freedom. Here we use deep learning to reveal tractable, low-dimensional representations of patterns in a canonical protein signaling process — the Rho-GTPase system — as well as complex Ginzburg-Landau dynamics. We show that our representations recover activity levels and irreversibility trends for a range of patterns. Additionally, we find that our irreversibility estimates serve as a dynamical order parameter, distinguishing stable and chaotic dynamics in these nonlinear systems. Our framework leverages advances in deep learning to quantify the nonequilibrium and nonlinear behavior of complex living processes.

## I. INTRODUCTION

Living matter consumes free energy through metabolism, forming patterns in processes such as development and motility [1–5]. These nonequilibrium processes violate governing principles of equilibrium systems, such as the Boltzmann distribution, impeding physical characterization [6]. These processes are nevertheless constrained by the second law of thermodynamics, as free-energy consumption measurably increases the entropy of the environment and accompanies broken detailed balance [7]. Broken detailed balance entails asymmetric transition rates between pairs of microstates, a time-reversal asymmetry enabling cycles in the phase space [8]. This asymmetry is also described as the “thermodynamic arrow of time”: concretely, the forward flow of events is distinguishable from its reverse [9]. The statistical distinguishability of time-forward and time-reversed processes in fact quantifies thermodynamic irreversibility [10]. Quantification of thermodynamic irreversibility is emerging as an important source of insight into nonequilibrium processes in biological and condensed-matter physics [11–15].

Irreversibility is measured as the Kullback-Leibler divergence (KLD) from the distribution of time-forward processes to the distribution of time-reversed processes, which requires sampling over many possible steady-state configurations. In practice, KLD estimates are constrained by the limited time-scales of experimental data and the complex interactions between many components and high dimensionality intrinsic to living systems. Reliable irreversibility estimates thus normally consider only a readily observed subset of degrees of freedom, such as time-resolved trajectories of probe particles [13]. However, recent deep-learning methods manipulate and synthesize complex data with ease, overcoming the curse of dimensionality inherent in statistical physics [16–19].

Neural networks can reduce high-dimensional signals to low-dimensional representations, potentially facilitating irreversibility quantification in complex living processes with many degrees of freedom.

Here we present a new framework based on disentangling variational neural networks to represent complex living processes as low-dimensional dynamics in a tractable latent feature space [20]. As proof of principle, we investigate nonequilibrium biochemical waves formed by Rho-GTPase signalling protein in the actomyosin cortex of the *Patiria miniata* (bat sea star) oocyte [21]. Using deep-learned feature-space representations, we recapitulate underlying irreversibility trends in both simulated and experimental Rho patterns. This suggests our framework provides a physically motivated indicator of activity in living systems. Moreover, our thermodynamic irreversibility estimates not only correctly rank the energetics of different patterns, but also serve as an order parameter indicating different dynamical regimes of this nonlinear system.

## II. RESULTS

### A. Complex Ginzburg-Landau dynamics describe the experimental Rho phase field

Evolutionarily conserved Rho GTPases play major roles in eukaryotic development [22]. Membrane-associated Rho self-organizes into waves of activation, with a range of nonequilibrium steady states visualizable using fluorescent reporters specific to active, GTP-bound Rho [Fig. 1(a) and Methods] [21]. Because Rho hydrolyzes GTP and diffuses down concentration gradients as it activates and inactivates, its reaction-diffusion wave patterning consumes chemical energy and is irreversible. Previous work indirectly inferred irreversibility in the Rho-regulated dynamics of sea-star oocytes using a subset of degrees of freedom [13]. Here we seek to directly quantify irreversibility from all information encoded in fluorescently labeled Rho.

\* These authors contributed equally to this work.

† Corresponding author: [fakhri@mit.edu](mailto:fakhri@mit.edu)

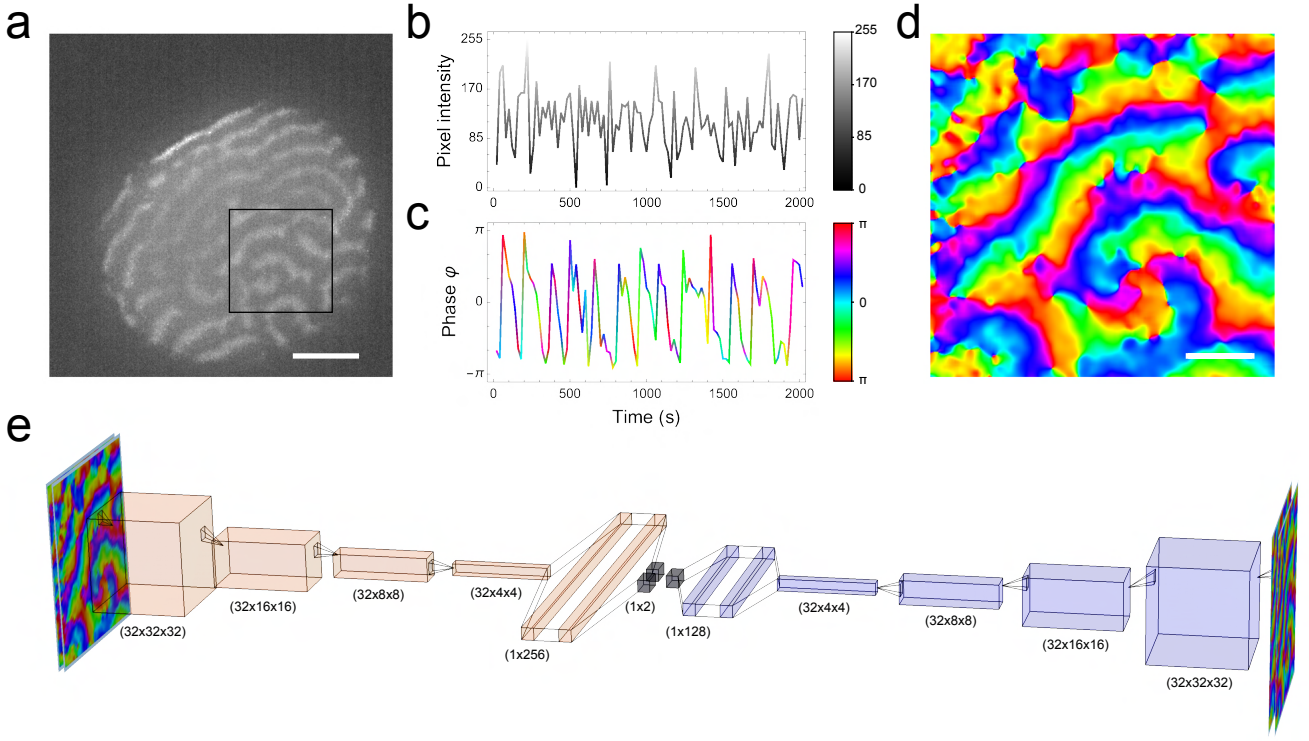


FIG. 1. The FVAE architecture represents Rho patterns. (a) Fluorescence micrograph shows GFP-labeled Rho-GTP forming spiral waves in the membrane of a starfish oocyte. Scale bar denotes  $50\mu\text{m}$ . (b) A pixel in (a) oscillates noisily over 2000 seconds. Intensity oscillations show fluctuating period and amplitude. (c) Relative-phase retrieval yields a clearly oscillatory signal from the intensity oscillation shown in (b). (d) Phase field of the boxed region in (a) retrieved by obtaining relative phases from all pixels as in (c). Scale bar denotes  $15\mu\text{m}$ . (e) The FVAE architecture (excluding discriminator, see Methods) represents and reconstructs inputs. The encoder (orange) feeds inputs through four convolutional layers and two linear layers to the bottleneck layers (grey). The first bottleneck layer represents variational posteriors as two  $1 \times 2$  vectors encoding the means and variances of two latent dimensions. The second bottleneck layer encodes  $1 \times 2$  vectors sampled from the variational posterior using reparameterization, which feed into the two linear layers and four transposed convolutional layers of the decoder (blue) to reconstruct inputs. FVAE inputs and outputs are  $2 \times 64 \times 64$  phase-field video segments, with channels for two successive frames.

To extract dynamics from noisy experimental data, we first converted Rho intensity fields captured through fluorescence microscopy into corresponding phase fields [21]. Rho activation alternating with inactivation results in intensity oscillations at each pixel [Fig. 1(b)], from which we retrieved relative phases [Fig. 1(c) and Methods]. Oscillations are more readily observed in phase fields than in intensity fields, which suffer fluctuations and envelope decay due to photobleaching and camera noise. For example, by repeating phase retrieval for all pixels in the boxed region of Fig. 1(a), we generated the phase field  $\varphi$  in Fig. 1(d).

Rho membrane dynamics are captured by the complex Ginzburg-Landau (CGL) equation [21]

$$\partial_t \varphi = \varphi + (1 + i c_1) \Delta \varphi - (1 + i c_2) |\varphi|^2 \varphi. \quad (1)$$

where  $\varphi$  is the phase,  $c_1$  models the linear dispersion of the medium, and  $c_2$  models the nonlinear dispersion. The CGL equation approximates envelope dynamics of reaction-diffusion patterning as arises in the well-known

Brusselator model [23, 24]. Intuitively, higher  $c_1$  corresponds to faster Rho diffusion, while higher  $c_2$  corresponds to higher Rho activation rate [25].

## B. Factorizing variational autoencoders represent high-dimensional dynamics in a low-dimensional latent space

Spatiotemporally continuous Rho phase fields, as in the CGL model, have many degrees of freedom and are challenging inputs for irreversibility estimators that take low-dimensional trajectories. Crucially, we use variational autoencoders (VAE) to represent Rho and CGL phase fields in low-dimensional latent spaces. Each VAE consists of an encoder, two bottleneck layers, and a decoder [Fig. 1(e) and Methods]. The encoder feeds inputs (here phase fields  $\varphi$ ) through convolutional layers followed by linear layers. Encoder outputs in the first bottleneck layer consist of means and variances of Gaus-

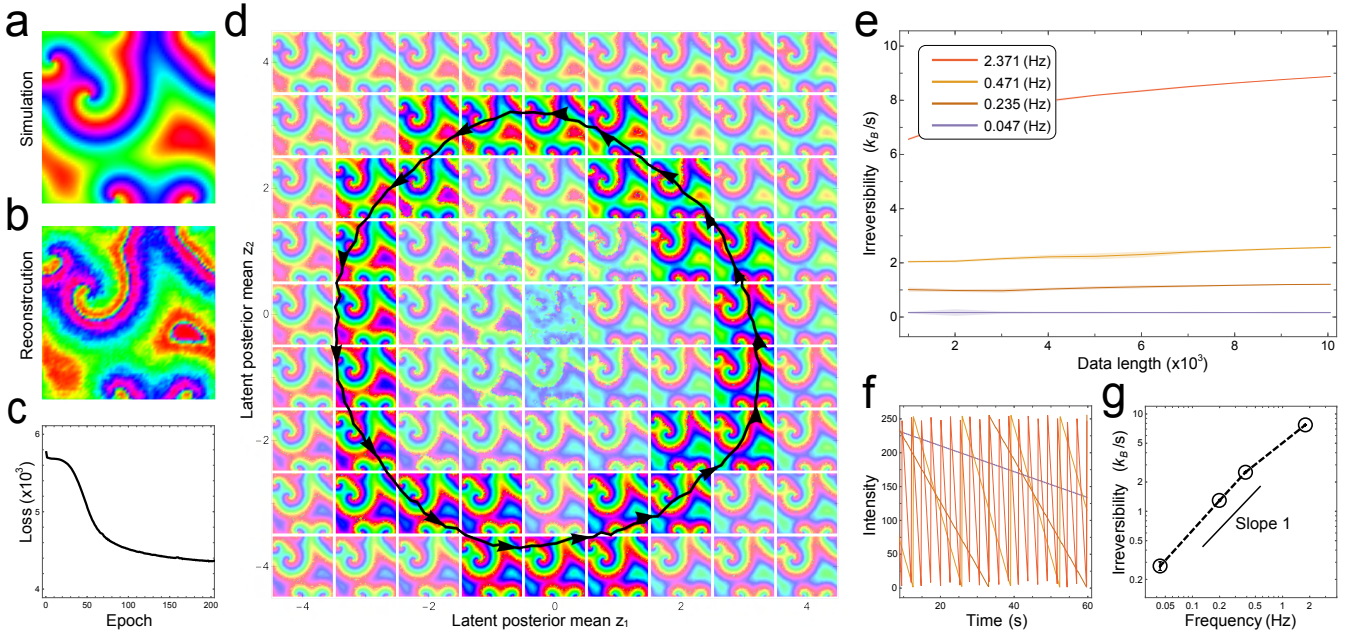


FIG. 2. Latent trajectories enable irreversibility estimates. (a) Snapshot of a simulated CGL pattern with  $c_1 = -0.2$  and  $c_2 = 0.5$ . (b) FVAE reconstruction of (a) after training. (c) Training loss (Eq. 2) decreases approximately monotonically with epochs. We terminate training when loss plateaus. (d) The trajectory (black curve) of the pattern with snapshot (a) traces a cycle in the latent space of an FVAE trained on the pattern’s segments. Arrows indicate direction. Background images are generated from their latent-space locations. Latent-space locations visited by the trajectory show highlighted reconstructions of the pattern. (e) ZM irreversibility estimates computed from simulation latent trajectories increase with frame rate (oscillation frequency). Shadowed regions indicate standard errors of means calculated over three independent simulations with the same dispersions. (f) Pixel-oscillation time series of simulations at the four frame rates shown in (e). (g) ZM estimates of simulations increase approximately linearly with oscillation frequencies shown in (e). Error bars indicate standard errors of means calculated over three independent simulations with the same dispersions.

sian variational posteriors  $q_\theta(\mathbf{z}|\varphi)$  over the  $d$ -dimensional latent space, where  $\theta$  denotes encoder parameters and  $\mathbf{z}$  denotes a latent-space vector. Decoder inputs in the second bottleneck layer are sampled from  $q_\theta(\mathbf{z}|\varphi)$  through reparameterization [26], and feed through linear layers followed by transposed convolutional layers. The decoder  $p_\phi(\varphi|\mathbf{z})$  outputs reconstructed  $\varphi$ , with  $\phi$  denoting decoder parameters.

For  $N$  inputs, we use a factorizing VAE (FVAE) loss function [20]

$$\begin{aligned} \frac{1}{N} \sum_{i=1}^N \{ & -\mathbb{E}_{q(\mathbf{z}|\varphi^{(i)})} [\ln p(\varphi^{(i)}|\mathbf{z})] \\ & + KL[q(\mathbf{z}|\varphi^{(i)})||\mathcal{N}(0, I)] \} \\ & + \gamma KL[q(\mathbf{z})|| \prod_{j=1}^d q(z_j)] \end{aligned} \quad (2)$$

with three terms. Here  $KL[\cdot||\cdot]$  denotes the KLD,  $\mathcal{N}(0, I)$  denotes a normal prior with  $I$  the  $d$ -dimensional identity matrix,  $q(\mathbf{z}) = \frac{1}{N} \sum_{i=1}^N q(\mathbf{z}|\varphi^{(i)})$  denotes the aggregate posterior, and  $q(z_j)$  denotes the aggregate-posterior marginal of  $z_j$ . The first term is a reconstruction error and measures the fidelity of FVAE reconstructions, while

the second term is a regularizer for penalizing model complexity. Weighted with a hyperparameter  $\gamma$ , the third term penalizes dependence between latent dimensions and encourages efficient (disentangled) representations (Table S1 and Methods). Training minimizes the loss in Eq. 2. Each input is two successive frames, and each phase-field video is segmented into overlapping inputs as one training batch to optimally capture pattern evolution. Main results use  $\gamma = 8$  and  $d = 2$  (Fig. S1 and Methods). By encoding high-dimensional inputs as variational posteriors in low-dimensional latent spaces, VAE can discover dynamical coordinates in nonlinear systems [27–30].

### C. Latent representations enable irreversibility estimates

Fig. 2(a) shows a simulated CGL phase-field frame with  $c_1 = -0.2$  and  $c_2 = 0.5$ , while Fig. 2(b) gives the corresponding FVAE reconstruction (Methods). The decoder faithfully reconstructs the input pattern from its latent representation. Due to the temporal periodicity of CGL patterns, random sets of phase-field video segments for training and validation are nearly identical. As a

result, we terminate training when regression over a window of epochs indicates that loss has ceased decreasing [Fig. 2(c) and Methods].

As the pattern evolves periodically, its variational-posterior mean exhibits cycles in the latent space [Fig. 2(d) and Fig. S2]. Tiles in Fig. 2(d) are decoded from lattice points in the latent space, with reconstructed frames highlighted along the pattern-evolution trajectory. Arrowheads denote points along the latent trajectory evenly spaced in time, and show increased speed in the latent space when the pattern evolves rapidly. FVAE latent dimensions are disentangled, and each row or column illustrates the effect of changing one latent variable, keeping the other fixed.

The unidirectional cycle in the latent space strongly indicates broken detailed balance and irreversible dynamics. Here we estimate irreversibility by applying the Ziv-Merhav (ZM) compression estimator [31] of KLD rates to forward and temporally reversed discretized latent trajectories (Fig. S3 and Methods) [32, 33]. Resulting ZM estimates are robust to choice of FVAE hyperparameters (Fig. S4). As the FVAE reconstructs with loss, latent trajectories do not encode full input information. ZM estimates computed from latent trajectories are thus lower bounds on irreversibility.

#### D. Irreversibility estimates reveal dynamical states

Estimating irreversibility from latent trajectories is data-efficient and computationally fast, as illustrated in Fig. 2(e). Note that CGL dynamics are deterministic, which results in irreversibility estimates that diverge logarithmically with increasing data length. However, relative divergence rates are different, enabling comparisons between differently evolving patterns (Fig. S5 and Supplementary Notes).

To test our framework, we simulated CGL patterns with the same dispersion parameters but different frame rates [Fig. 2(f) and Methods]. Intuitively, irreversibility should increase with oscillation frequency. The approximately linear increase in estimated irreversibility with frequency, shown in Fig. 2(g), suggests our framework successfully detects altered temporal structure and correctly orders nonequilibrium steady states by activity level.

Patterns differing by more than temporal frequency present additional challenges in irreversibility comparisons. The CGL model forms patterns with diverse spatial structures, such as those in Fig. 3(a). Spatial frequency increases with nonlinear dispersion  $c_2$  in the CGL equation and with effective kinetics in the Rho system [22]. We adapted our framework to compare irreversibilities of CGL dynamics and Rho patterns that differ in spatial structure.

Consider the latent trajectory in Fig. 2(d). Its speed increases when the pattern's spatial structures evolve more rapidly. Similar observations across trajectories

suggest that latent-space distance scales with pattern-space distance: the L2 distance between a first phase-field video segment and successive segments is approximately proportional to the corresponding L2 distance between the first segment's variational-posterior mean and successive segments' variational-posterior means [Fig. 3(b)]. In agreement with the Johnson-Lindenstrauss lemma [34], relative L2 distances are preserved between input pattern segments and their latent representations. The VAE obeys a Lipschitz property [35, 36]

$$\|\mathbf{z} - \mathbf{z}'\| \leq C\|\varphi - \varphi'\| \quad (3)$$

where  $\mathbf{z}$  and  $\mathbf{z}'$  are two latent vectors,  $\varphi$  and  $\varphi'$  are the corresponding input phase patterns,  $C > 0$  is a real constant, and  $\|\cdot\|$  denotes the L2 norm.

Accordingly, we add a phase-zero (vanishing-field) phase-field video segment to all training sets as a reference: the reference is mapped close to the origin in latent spaces. Comparing L2 distances to the reference in pattern and latent spaces [Fig. 3(c)], we rescale latent trajectories to a constant distance ratio shared between models trained on different patterns (Methods). Applying the ZM estimator to rescaled trajectories, irreversibilities increase with  $c_2$  at constant  $c_1$ . Results in Fig. 3(d) corroborate the notion that nonequilibrium potentials increase with complexity in patterns excited from homogeneous media [23], as well as with the interpretation of  $c_2$  as modeling Rho-pathway activity level.

In intriguing agreement with simulations, experiments show irreversibility estimates initially increasing with pattern complexity across states numbered by effective kinetic energy, a measure of Rho activation rate [Fig. S6 and Methods] [25]. However, irreversibility estimates decrease sharply above a critical Rho activation rate [curve in Fig. 4(a)]. Rho patterns enter a chaotic regime, where stable spiral waves do not arise [21] [insets in Fig. 4(a)]. This chaotic regime also occurs in CGL dynamics above a critical nonlinear dispersion  $c_2$  or below a critical linear dispersion  $c_1$  [Fig. 4(b)]. The transition between stable spirals and chaotic turbulence can be detected through linear stability analysis of the CGL equation [37, 38]. Interestingly, we recover this transition in estimated irreversibilities of patterns simulated at different dispersions [Fig. 4(c)]. The nearly vanishing irreversibility estimates in the chaotic regime are counter-intuitive, but may be explained as follows: 1) In the stable regime, long-lived waves are a major and readily detected source of irreversibility. However, the chaotic regime lacks structured wave-like motion: irreversibility might instead arise from higher-order correlations and non-exponential waiting times [39, 40]. Nonzero irreversibility estimates are thus difficult to obtain numerically. 2) The CGL equation describes a reaction-diffusion system with a reaction network not captured fully by the Rho phase field. Chaos occurs at high nonlinear dispersion, which may correspond to more irreversibility arising in unobserved parts of the reaction pathway [23, 41]. 3) Chaotic patterns are unpredictable and susceptible to initial conditions

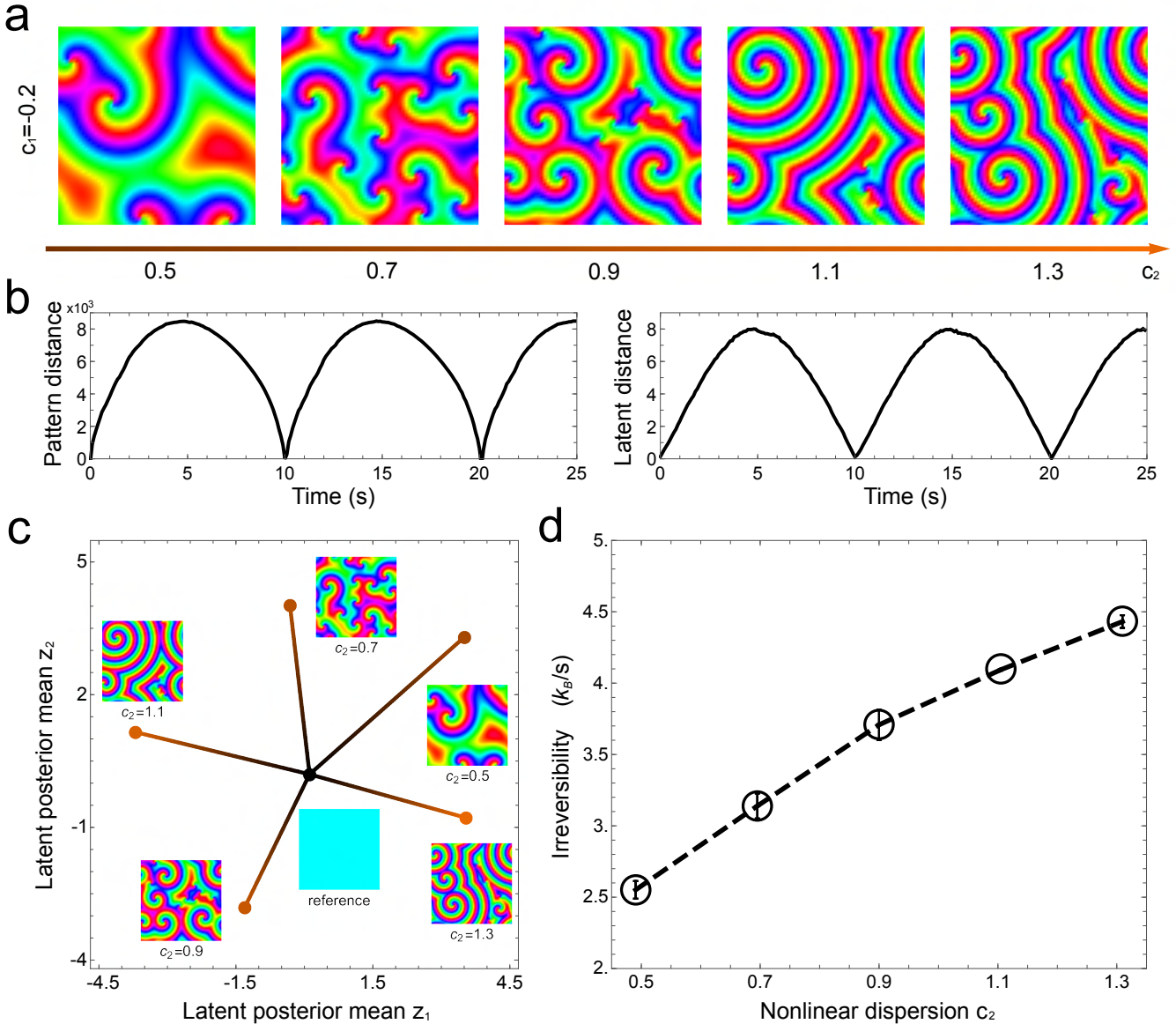


FIG. 3. Rescaled latent representations enable irreversibility comparison between patterns differing in spatial structure. **a.** Patterns with higher  $c_2$  exhibit higher spatial frequencies. Snapshots show phase fields of patterns with linear dispersion  $c_1 = -0.2$  fixed and nonlinear dispersion  $c_2$  varying in increments of 0.2 between 0.5 and 1.3. **b.** A pattern's distances in phase-field space are approximately proportional to corresponding distances in the latent space of a model trained on that pattern. Left panel shows the L2 norm between the first and successive segments in a simulation with  $c_1 = -0.2$  and  $c_2 = 0.5$  [Fig. 2(a)]; right panel shows the L2 norm between variational-posterior means of those segments. **c.** Absolute latent distance from a vanishing-field reference does not reflect relative pattern complexity between models trained on different patterns. Distances are shown between the five representative segments in **a** and the vanishing-field reference in the superimposed latent spaces of FVAE trained on each simulation. **d.** Irreversibility estimates increase with nonlinear dispersion  $c_2$  and pattern complexity at fixed linear dispersion  $c_1$ . Means and error bars indicate averages and standard errors over three independent simulation replicates.

not captured in a few latent dimensions. Reconstruction loss is greater for chaotic patterns than for stable patterns (Fig. S7). Following these observations, we propose our irreversibility estimates as a dynamical order parameter distinguishing stable and chaotic regimes in nonlinear systems. Lastly, at fixed nonlinear dispersion

$c_2$ , decreasing linear dispersion  $c_1$  increases pattern complexity while decreasing irreversibility estimates [leftmost column, Fig. 4(c)]. This behavior arises because irreversibility depends on both spatial and temporal structure: decreasing linear dispersion  $c_1$  increases spatial frequency, but also decreases temporal frequency.

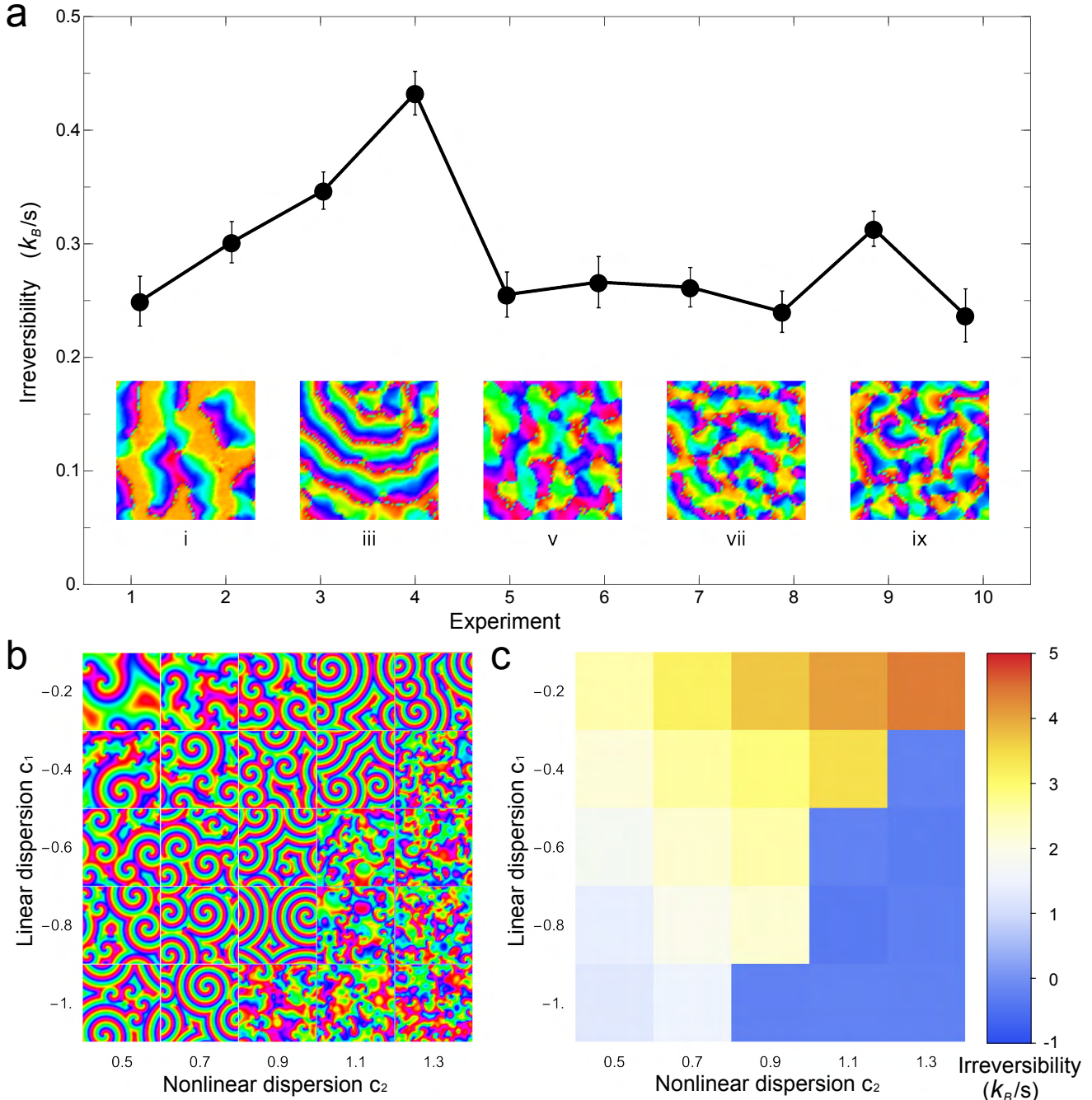


FIG. 4. Irreversibility estimates distinguish dynamical regimes of Rho and CGL pattern formation. **a.** Irreversibility estimates increase with activity for experimental Rho states in the stable regime, but not upon transitioning to the chaotic regime. Error bars indicate standard errors of averages over training seeds (Fig. S8 and Methods). Experimental Rho states are numbered by increasing effective kinetic energy (Fig. S6 and Methods). Numbered insets show selected states. **b.** The CGL model exhibits stable and chaotic regimes. Simulation snapshots are shown for varying dispersions. The chaotic regime lacking spiral waves is shown in the lower right. **c.** Stable-regime CGL simulations show irreversibility estimates increasing with dispersion parameters  $c_1$  and  $c_2$ . Chaotic-regime CGL simulations show vanishing irreversibility estimates. Irreversibilities are estimated from FVAE latent trajectories for CGL simulations of varying dispersion parameters.

### III. DISCUSSION

In conclusion, we combine variational autoencoder networks with thermodynamic inference to robustly esti-

mate and compare irreversibilities in spatiotemporally evolving biological patterns. Moreover, our framework reveals key features of simulated CGL and experimen-

tal oocyte-Rho dynamics, including stability transitions between cell patterns and relative cell-activity levels. Because our framework does not rely on prior knowledge of system dynamics, we expect that it is applicable to general high-dimensional biological time series. With irreversibility ubiquitous out of equilibrium, our framework could rank activity levels and unveil dynamical properties, such as stability, in a broad range of living systems. As our framework discovers efficient latent representations characterizing complex systems, these systems' underlying dynamics might be captured by a few degrees of freedom. Physical interpretation of latent dimensions provides an intriguing avenue for understanding the origins of observed irreversibility.

## IV. METHODS

### A. Rho data acquisition

Experimental videos of Rho-GTP wave patterns were obtained from a previous study [21]. In brief, *Patiria miniata* (bat sea star) oocytes were extracted and washed with filtered seawater. Two constructs, eGFP-rGBD for labeling Rho-GTP molecules and Ect2-T808A-mCherry for generating excitable Rho-GTP cortical waves, were microinjected into the cytoplasm of the oocytes before incubation overnight at 15°C. Microinjected oocytes were treated with 10 μM 1-methyl adenine solution to induce meiosis and then loaded into customized polydimethylsiloxane (PDMS) chambers to minimize positional drift during imaging. To collect near-membrane Z-stack signals, time-lapse confocal images were acquired using a ×40/NA 1.3 oil Plan Apochromat objective with appropriate laser lines and emission filters. Ten steady-state Rho patterns were recorded during ten contraction events over seven oocytes.

### B. Data processing

We first obtain nonoverlapping 128 × 128-pixel crops from raw intensity data. Phase field  $\varphi(x, t)$  is calculated at each pixel over the entire 2D image. In order to minimize noise, we also performed background subtraction with a moving average over 15 frames. We finally performed average pooling over 2 × 2-pixel kernels to generate 64 × 64-pixel phase-field images.

To rank cell-activity level, we calculated effective kinetic energies of different Rho phase patterns from corresponding phase-velocity fields:  $V_\varphi(x, t) = \nabla \varphi(x, t)$ . The effective kinetic energy is defined simply as  $\langle |V_\varphi(x, t)|^2 \rangle$  with  $\langle \dots \rangle$  denoting an average over both space and time (Fig. S6).

### C. FVAE objective

The FVAE objective function (negative loss function Eq. 2) is as previously described [20]. In brief, we assume that  $N$  observations  $\varphi^{(i)} \in \Phi, i = 1, \dots, N$  are generated by combining  $K$  independent underlying factors of variation  $\mathbf{f} = (f_1, \dots, f_K)$ . The FVAE uses real-valued latent vectors  $\mathbf{z} \in \mathbb{R}^d$  to represent observations. The generative model is defined by a standard Gaussian prior  $p(\mathbf{z}) = \mathcal{N}(0, I)$ , where  $I$  is a  $d$ -dimensional identity matrix. For each observation, the encoder produces the mean  $\mu_j(\varphi)$  and variance  $\sigma_j^2(\varphi)$  of variational posterior  $q_\theta(\mathbf{z}|\varphi) = \prod_{j=1}^d \mathcal{N}(z_j | \mu_j(\varphi), \sigma_j^2(\varphi))$  parameterized by neural network  $\theta$ . The decoder  $p_\phi(\varphi|\mathbf{z})$  is parameterized by neural network  $\phi$ . Considering all observations in the dataset, the distribution of latent representations is

$$q(\mathbf{z}) = \mathbb{E}_{p_{\text{obs}}(\varphi)}[q(\mathbf{z}|\varphi)] = \frac{1}{N} \sum_{i=1}^N q(\mathbf{z}|\varphi^{(i)}), \quad (4)$$

where  $p_{\text{obs}}(\varphi)$  is the empirical distribution.

In a standard VAE, the evidence lower bound objective (ELBO):

$$\frac{1}{N} \sum_{i=1}^N \mathbb{E}_{q(\mathbf{z}|\varphi^{(i)})}[\ln p(\varphi^{(i)}|\mathbf{z})] - KL[q(\mathbf{z}|\varphi^{(i)})||\mathcal{N}(0, I)] \quad (5)$$

bounds the log-likelihood from below. The first term of Eq. 5 is a negative reconstruction (binary cross entropy) loss, while the second term containing the Kullback-Leibler (KL) divergence

$$KL[p||q] = \mathbb{E}_p[\ln \frac{p}{q}] \quad (6)$$

is a regularizer for model complexity.

To learn latent factors encoding complementary subsets of the  $d$  mutually independent  $\mathbf{f}$ , the FVAE objective function subtracts a total correlation (TC)

$$\gamma KL[q(\mathbf{z})||\bar{q}(\mathbf{z})] \quad (7)$$

where

$$\bar{q}(\mathbf{z}) = \prod_{j=1}^d q(z_j) \quad (8)$$

and  $\gamma$  is a constant hyperparameter greater than unity [42]. The TC penalizes dependence between latent dimensions as the KL divergence between the aggregate posterior  $q(\mathbf{z})$  and the product of aggregate-posterior marginals  $\bar{q}(\mathbf{z})$ . Samples of  $q(\mathbf{z})$  are obtained by sampling a batch of  $q(\mathbf{z}|\varphi^{(i)})$ . Samples of the product of aggregate-posterior marginals are obtained by randomly permuting each latent variable across a sampled batch of

$q(\mathbf{z}|\varphi^{(i)})$ , approximating  $\bar{q}(\mathbf{z})$  in large batches [43]. A discriminator  $D$  training to distinguish between samples of  $q(\mathbf{z})$  and  $\bar{q}(\mathbf{z})$  outputs an estimate  $D(\mathbf{z})$  that each sample belongs to  $q(\mathbf{z})$ . The TC is thereby approximated as

$$KL[q(\mathbf{z})||\bar{q}(\mathbf{z})] \approx \mathbb{E}_{q(\mathbf{z})} \ln \frac{D(\mathbf{z})}{1 - D(\mathbf{z})} \quad (9)$$

in computing the VAE loss function during joint training with the discriminator  $D$  [44, 45].

#### D. FVAE architecture

Each FVAE consists of a VAE and a discriminator. We adapted our architecture from open source code using the PyTorch machine-learning package [46, 47]. The VAE has a feedforward architecture, with signals passing sequentially through the encoder, bottleneck, and decoder [Fig. 1(e)]. The encoder comprises four convolutional layers followed by two 256-unit linear layers. The bottleneck comprises a 4-unit linear layer, encoding means and variances of variational posteriors in two-dimensional latent space, followed by a 2-unit linear layer, encoding latent-space vectors sampled from the variational posterior through reparameterization [26]. The decoder comprises two 128-unit linear layers followed by four transposed convolutional layers. All convolutional and transposed convolutional layers have 1-pixel dilation, 1-pixel padding, 2-pixel stride, and  $4 \times 4$ -pixel kernel. This architecture is largely as previously described [48]. However, we use 4-unit and 2-unit bottleneck layers for two-dimensional latent spaces instead of 20-node and 10-node bottleneck layers for ten-dimensional latent spaces. Models were initially trained with a larger number of latent dimensions (Fig. S1). Models trained on simulations of stable CGL dynamics often converge on two-dimensional models: the number of latent dimensions was set to two to facilitate comparison between final models. Moreover, we use a sigmoid activation in the final layer of the decoder. The VAE otherwise uses ReLU activations. The discriminator is a previously described perceptron with six 1000-unit layers using leaky ReLU activations of negative-domain slope 0.2 [20].

#### E. FVAE training

Inputs are  $2 \times 64 \times 64$ -pixel TIFF image stacks formatted into PyTorch tensors. Each input is a two-frame observation of spatiotemporal dynamics in CGL phase-field video or phase-field video extracted from fluorescence micrographs of GFP-labeled active Rho in a starfish-oocyte actomyosin cortex. Each dataset consists of all such two-frame segments of a video in addition to a  $2 \times 64 \times 64$  vanishing-field reference segment. Outputs are  $2 \times 64 \times 64$  tensors, and are input reconstructions or generated by decoding latent-space vectors. During each training epoch,

the dataset was randomly split into two equally sized batches, one for the VAE and the other for the discriminator. For each model, parameters were updated by backpropagation until FVAE loss stopped decreasing. Each epoch, FVAE loss was evaluated for the entire dataset: regression was performed on the average losses over a hyperparameter “window” of previous epochs. If the resulting slope was not significantly less than zero at 95 percent confidence level for a hyperparameter “stop” number of consecutive epochs, training was stopped.

Training hyperparameters were selected by hyperparameter tuning [49]. To determine whether hyperparameters affect estimated irreversibilities, additional models were trained each with one hyperparameter decreased or increased by a factor of two from its default value (Table S1). Such models were trained for higher and lower values of each training hyperparameter on a simulation dataset ( $c_1 = -0.2$ ,  $c_2 = 0.5$ , timestep 0.1, and initialization seed 0) and an experiment dataset (crop 1 of experiment  $i$ ): estimated irreversibilities vary little with choice of hyperparameters, but are more variable for experiments than for simulations (Fig. S4).

One model was trained for each simulation dataset using a training seed of 1234. Some models trained on simulations produced discontinuous (non-Lipschitz) encodings: these models result in lower estimated irreversibilities, and are readily visually identified by examining latent trajectories (Fig. S2). These models were rejected as they do not reflect the continuity of CGL dynamics, and models were retrained for their datasets using new training seeds (1243 or 1324). However, discontinuous encodings are not readily identified in models trained on experimental datasets, which are smaller than simulation datasets, have lower frame rate, and describe dynamics not in long-term steady states: these datasets result in latent trajectories not as “smooth” as those of models trained on simulation datasets. To address the effects of possible discontinuous encodings, twelve models with different training seeds (1234, 1243, 1324, 1342, 1423, 1432, 2134, 2143, 2314, 2341, 2413, and 2431) were trained for each experimental dataset, with irreversibilities then averaged.

All models were trained on an Nvidia Titan RTX graphics card with CUDA driver.

#### F. CGL phase-field simulations

Complex Ginzburg-Landau phase-fields were simulated in MATLAB using ETD2 exponential time differencing [50, 51]. Random initial conditions were evolved for  $10^6$  time steps, with the last  $10^4$  time steps retained. For most simulations, linear and nonlinear dispersion parameters  $c_1$  and  $c_2$  were varied in increments of 0.2 over  $[-1.0, -0.2]$  and  $[0.5, 1.3]$ , respectively, at a time-step length of 0.10. In Fig. 2, simulations were performed at time-step lengths  $\{0.01, 0.05, 0.10, 0.50\}$  for the CGL equation with  $c_1 = -0.2$  and  $c_2 = 0.5$ . The first three

seeds to result in simulations reaching steady states (constant pixel oscillation envelopes) were used for each set of CGL dispersion parameters and time-step lengths. Simulations were performed on a 3.3 GHz Quad-Core Intel Core i5 device.

### G. ZM compression estimator

Our Ziv-Merhav compression estimator is as previously described [33]. For any time-series trajectory  $\underline{z} = \{\underline{z}^{(1)}, \underline{z}^{(2)}, \dots, \underline{z}^{(N)}\}$  and its reverse  $\tilde{\underline{z}} = \{\underline{z}^{(N)}, \underline{z}^{(N-1)}, \dots, \underline{z}^{(1)}\}$ , the ZM estimator is

$$\hat{S}_{\text{ZM}} = \frac{1}{N} [c_r(\underline{z}|\tilde{\underline{z}}) \ln N - c(\underline{z}) \ln c(\underline{z})]. \quad (10)$$

The first term in Eq. 10 is the cross entropy rate, where  $c_r(\underline{z}|\tilde{\underline{z}})$  is defined as the length after parsing the forward trajectory  $\underline{z}$  by its reverse  $\tilde{\underline{z}}$  using the Lempel-Ziv (LZ) algorithm [31]. This term is also known as the cross-parsing length. The second term is the Shannon entropy rate and  $c(\underline{z})$  denotes the length of  $\underline{z}$  after compressing with the LZ algorithm. To improve performance with limited data, we correct our estimator by applying it to half trajectories

$$\hat{S}_{\text{half}} = \frac{1}{N/2} [c_r(\underline{z}_{N/2}^N|\tilde{\underline{z}}_1^{N/2}) \ln N/2 - c(\underline{z}_{N/2}^N) \ln c(\underline{z}_{N/2}^N)] \quad (11)$$

and subtracting the asymptotically vanishing component

$$\hat{S}_{\text{corr}} = \hat{S}_{\text{ZM}} - \hat{S}_{\text{half}}, \quad (12)$$

again as previously described [33].

Since latent trajectories are of high precision, they are barely compressible. In order to use the ZM compression estimator, we first discretize our latent trajectories using the floor function  $\lfloor z/b \rfloor$ , with  $b$  the parameter controlling discretization [Fig. S3(a)-(c)]. Although irreversibility estimates are higher for finer discretizations, the trend across regimes is preserved [Fig. S3(d)-(e)]. With enough

data, different discretizations scale irreversibility estimates without altering their rankings. All main results are calculated with  $b = 1$ .

### H. Latent-trajectory rescaling

Since our VAE obeys a Lipschitz property (Eq. 3), we rescale the latent trajectories of different patterns by the patterns' distances to a vanishing-field reference as

$$z_{\text{rescale}} = \frac{\langle \|\varphi - \varphi_0\| \rangle}{1000 \langle \|z - z_0\| \rangle} z. \quad (13)$$

Here  $\varphi_0$  is the reference and  $z_0$  is its position in a latent space after training.  $\langle \cdot \rangle$  denotes a time average over the entire simulation or experiment.

## DATA AVAILABILITY

All data and code supporting this study are available for download at <https://doi.org/10.5281/zenodo.7734339> and <https://doi.org/10.5281/zenodo.7737963>, respectively.

## AUTHOR CONTRIBUTIONS

J.L., C.-W.J.L., and N.F. designed research. J.L., C.-W.J.L., and M.S. performed research. J.L., C.-W.J.L., and M.S. contributed new reagents/analytic tools. J.L. and C.-W.J.L. analyzed data. J.L., C.-W.J.L., and N.F. wrote the paper.

## ACKNOWLEDGMENTS

We thank Jinghui Liu and Tzer Han Tan for help in data acquisition, Jordan M. Horowitz and Sarah E. Marzen for comments on the manuscript, and Hong-Hsing Liu for sharing compute resources. This work was supported by National Science Foundation CAREER Grant No. PHYS-1848247 (to N.F.) and Alfred P. Sloan Foundation Grant G-2021-16758 (to N.F.).

---

[1] D. Needleman and Z. Dogic, *Nature Reviews Materials* **2**, 17048 (2017).

[2] F. Gnesotto, F. Mura, J. Gladrow, and C. Broedersz, *Reports on Progress in Physics* **81**, 066601 (2018).

[3] M. C. Marchetti, J.-F. Joanny, S. Ramaswamy, T. B. Liverpool, J. Prost, M. Rao, and R. A. Simha, *Reviews of Modern Physics* **85**, 1143 (2013).

[4] U. Seifert, *Reports on Progress in Physics* **75**, 126001 (2012).

[5] A. Murugan and S. Vaikuntanathan, *Journal of Statistical Physics* **162**, 1183 (2016).

[6] G. E. Crooks, *Physical Review E* **60**, 2721 (1999).

[7] D. Loposchainsky and H. Hinrichsen, *Journal of Statistical Physics* **153**, 828 (2013).

[8] C. Battle, C. P. Broedersz, N. Fakhri, V. F. Geyer, J. Howard, C. F. Schmidt, and F. C. MacKintosh, *Science* **352**, 604 (2016).

[9] A. Seif, M. Hafezi, and C. Jarzynski, *Nature Physics* **17**, 105 (2021).

[10] J. M. R. Parrondo, C. Van den Broeck, and R. Kawai, *New Journal of Physics* **11**, 073008 (2009).

[11] J. Li, J. M. Horowitz, T. R. Gingrich, and N. Fakhri, *Nature Communications* **10**, 1 (2019).

[12] T. H. Tan, A. Mietke, J. Li, Y. Chen, H. Higinbotham, P. J. Foster, S. Gokhale, J. Dunkel, and N. Fakhri, *Nature* **607**, 287 (2022).

[13] T. H. Tan, G. A. Watson, Y.-C. Chao, J. Li, T. R. Gingrich, J. M. Horowitz, and N. Fakhri, arXiv preprint arXiv:2107.05701 [10.48550/arXiv.2107.05701](https://arxiv.org/abs/2107.05701) (2021).

[14] T. R. Gingrich, J. M. Horowitz, N. Perunov, and J. L. England, *Physical Review Letters* **116**, 120601 (2016).

[15] U. Seifert, *Annual Review of Condensed Matter Physics* **10**, 171 (2019).

[16] Y. Bahri, J. Kadmon, J. Pennington, S. S. Schoenholz, J. Sohl-Dickstein, and S. Ganguli, *Annual Review of Condensed Matter Physics* **11**, 10.1146/annurev-conmatphys-031119-050745 (2020).

[17] B. Lusch, J. N. Kutz, and S. L. Brunton, *Nature Communications* **9**, 1 (2018).

[18] M. J. Falk, V. Alizadehyazdi, H. Jaeger, and A. Murugan, *Physical Review Research* **3**, 033291 (2021).

[19] M. S. Schmitt, J. Colen, S. Sala, J. Devany, S. Seetharaman, M. L. Gardel, P. W. Oakes, and V. Vitelli, *Zyxin is all you need: machine learning adherent cell mechanics* (2023).

[20] H. Kim and A. Mnih, in *International Conference on Machine Learning* (PMLR, 2018) pp. 2649–2658.

[21] T. H. Tan, J. Liu, P. W. Miller, M. Tekant, J. Dunkel, and N. Fakhri, *Nature Physics* **16**, 657 (2020).

[22] M. C. Wigbers, T. H. Tan, F. Brauns, J. Liu, S. Z. Swartz, E. Frey, and N. Fakhri, *Nature Physics* **17**, 578 (2021).

[23] G. Falasco, R. Rao, and M. Esposito, *Physical Review Letters* **121**, 108301 (2018).

[24] Y. Kuramoto, *Chemical Oscillations, Waves, and Turbulence* (Springer, 1984) pp. 111–140.

[25] J. Liu, J. F. Totz, P. W. Miller, A. D. Hastewell, Y.-C. Chao, J. Dunkel, and N. Fakhri, *Proceedings of the National Academy of Sciences* **118**, e2104191118 (2021).

[26] D. P. Kingma and M. Welling, *Auto-encoding variational bayes* (2013).

[27] H. Gabbard, C. Messenger, I. S. Heng, F. Tonolini, and R. Murray-Smith, *Nature Physics* **18**, 112 (2021).

[28] C. Miles, M. R. Carbone, E. J. Sturm, D. Lu, A. Weichselbaum, K. Barros, and R. M. Konik, *Physical Review B* **104**, 235111 (2021).

[29] N. Takeishi and A. Kalousis, in *Advances in Neural Information Processing Systems*, Vol. 34, edited by M. Ranzato, A. Beygelzimer, Y. Dauphin, P. Liang, and J. W. Vaughan (Curran Associates, Inc., 2021) pp. 14809–14821.

[30] J. Wang, C. He, R. Li, H. Chen, C. Zhai, and M. Zhang, *Physics of Fluids* **33**, 086108 (2021).

[31] J. Ziv and A. Lempel, *IEEE Transactions on Information Theory* **23**, 337 (1977).

[32] É. Roldán and J. M. R. Parrondo, *Physical Review Letters* **105**, 150607 (2010).

[33] É. Roldán and J. M. R. Parrondo, *Physical Review E* **85**, 031129 (2012).

[34] W. B. Johnson and J. Lindenstrauss, *Contemporary Mathematics* **26**, 28 (1984).

[35] K. Sun, J. Zhang, C. Zhang, and J. Hu, *Neurocomputing* **230**, 374 (2017).

[36] A. Camuto and M. Willetts, in *International Conference on Artificial Intelligence and Statistics* (PMLR, 2022) pp. 4595–4611.

[37] I. S. Aranson and L. Kramer, *Reviews of Modern Physics* **74**, 99 (2002).

[38] H. Chaté and P. Manneville, *Physica A: Statistical Mechanics and its Applications* **224**, 348 (1996).

[39] C. W. Lynn, C. M. Holmes, W. Bialek, and D. J. Schwab, *Physical Review Letters* **129**, 118101 (2022).

[40] D. J. Skinner and J. Dunkel, *Physical Review Letters* **127**, 198101 (2021).

[41] Q. Yu, D. Zhang, and Y. Tu, *Physical Review Letters* **126**, 080601 (2021).

[42] S. Watanabe, *IBM Journal of Research and Development* **4**, 66 (1960).

[43] M. A. Arcones and E. Gine, *Annals of Statistics* **20**, 655 (1992).

[44] X. Nguyen, M. J. Wainwright, and M. I. Jordan, *IEEE Transactions on Information Theory* **56**, 5847 (2010).

[45] M. Sugiyama, T. Suzuki, and T. Kanamori, *Annals of the Institute of Statistical Mathematics* **64**, 1009 (2012).

[46] Y. Dubois, A. Kastanos, D. Lines, B. Melman, and G. Eraslan, *Disentangled vae*, <https://github.com/YannDubs/disentangling-vae> (2021).

[47] A. Paszke, S. Gross, F. Massa, A. Lerer, J. Bradbury, G. Chanan, T. Killeen, Z. Lin, N. Gimelshein, L. Antiga, A. Desmaison, A. Kopf, E. Yang, Z. DeVito, M. Raison, A. Tejani, S. Chilamkurthy, B. Steiner, L. Fang, J. Bai, and S. Chintala, in *Advances in Neural Information Processing Systems 32*, edited by H. Wallach, H. Larochelle, A. Beygelzimer, F. d'Alché-Buc, E. Fox, and R. Garnett (Curran Associates, Inc., 2019) pp. 8024–8035.

[48] C. P. Burgess, I. Higgins, A. Pal, L. Matthey, N. Watters, G. Desjardins, and A. Lerchner, in *NIPS Workshop on Learning Disentangled Representations* (arXiv, 2018).

[49] I. Goodfellow, Y. Bengio, and A. Courville, *Deep Learning* (MIT Press, Cambridge, MA, 2016).

[50] S. Cox and P. Matthews, *Journal of Computational Physics* **176**, 430 (2002).

[51] D. M. Winterbottom, The complex ginzburg-landau equation, <https://github.com/codeinthehole/codeinthehole.com/blob/58ad3d28ddefb64350ec883b291d4dbe1df096f7/www/static/tutorial/files/CGLsim2D.m> (2005).

## SUPPLEMENTARY NOTES

### DIVERGENCE OF ZM ESTIMATOR ON DETERMINISTIC PROCESSES

As CGL dynamics are deterministic, stochastic reverse processes are not observed. Irreversibilities of deterministic processes should diverge, raising the question of how such diverging irreversibilities can be compared. Applied to a trajectory of finite length, the ZM estimator of irreversibility is finite [10, 32, 33]. For deterministic trajectories, these estimates diverge logarithmically at different rates, allowing comparison.

Fig. S5(a) shows an example trajectory following deterministic dynamics:

$$\begin{aligned} x &= r \cos(\omega t - \pi/4) \\ y &= -r \sin(\omega t - \pi/4), \end{aligned} \quad (\text{S1})$$

with  $r = 0.9$ ,  $\omega = \pi/2$ , and time step 1. As described in Methods, we discretize this trajectory with  $b = 1$  to apply the ZM estimator. As a result, this trajectory can be labeled as a series of discrete positions  $\underline{z} = \{1, 2, 3, 4, 1, 2, 3, 4, 1, 2, 3, 4, \dots\}$ . For simplicity, we assume the series is finite with length  $4N$  ( $N \gg 4$ ) and its reverse is  $\tilde{\underline{z}} = \{4, 3, 2, 1, 4, 3, 2, 1, 4, 3, 2, 1, \dots\}$ . Plugging this series and its reverse into Eq. 10, we derive the cross parsing length  $c_r(\underline{z}|\tilde{\underline{z}}) = 4N$ , the compression length  $c(\underline{z}) \approx \log_2 4N$ , and the ZM compression estimator

$$\hat{S}_{\text{ZM}} \approx \ln 4N - \frac{\log_2 4N}{4N}. \quad (\text{S2})$$

As  $N \rightarrow \infty$ , we can see that  $\hat{S}_{\text{ZM}} \rightarrow \ln 4N$  and diverges logarithmically as shown in Fig. S5(e). However, if the dynamics in Eq. S1 are slower with  $\omega = \pi/6$ , the discretized trajectory becomes  $\underline{z} = \{1, 1, 1, 2, 2, 2, 3, 3, 3, 4, 4, 4, \dots\}$  [Fig. S5(b)]. The resulting ZM estimator  $\hat{S}_{\text{ZM}} \rightarrow \frac{\ln 4N}{3}$  [Fig. S5(f)]. Although the estimated irreversibility will eventually diverge, for a trajectory of the same finite length, it is one third that of the faster-evolving case shown in Fig. S5(a). This property helps us to distinguish and compare different temporal structures in main text Fig. 2.

We can similarly compare different spatial structures. In Fig. S5(c), we dilated the trajectory in Fig. S5(b) with  $\omega = \pi/6$  and  $r = 1.5$ . Indeed, the ZM estimate for the trajectory in Fig. S5(c) is greater than that for the trajectory in Fig. S5(b) with the same trajectory length and discretization [Fig. S5(g)]. More precisely, the long-time finite ZM estimate shown in Fig. S5(g) is three times that shown in Fig. S5(f). This is because, though the trajectories in Fig. S5(b) and Fig. S5(c) have the same period, the latter trajectory visits three times as many distinct discretized positions as the former: it is one third as compressible using its reverse. Moreover, the finite ZM estimator also captures different trajectory geometries. The elliptical dynamics shown in Fig. S5(d), which follow  $x = 0.9 \cos(\pi t/6 - \pi/4)$  and  $y = -1.5 \sin(\pi t/6 - \pi/4)$ , will evolve at different speeds along the trajectory. The spatially varying trajectory speed increases the compressibility of the trajectory, as only eight distinct discretized positions are visited, and is manifested in the ZM estimator [Fig. S5(h)]. As a result, we are able to compare the irreversibilities of different spatial structures in main text Fig. 3.

Altogether, we conclude that even for deterministic processes, the finite-trajectory ZM estimator still distinguishes and enables comparisons between dynamics.

TABLE S1. Default training-hyperparameter values.

Hyperparameter	Simulation models	Experiment models
VAE learning rate (vaelr)	$1 \times 10^{-3}$	$1 \times 10^{-3}$
Discriminator learning rate (dlr)	$5 \times 10^{-5}$	$5 \times 10^{-5}$
TC coefficient $\gamma$ (fg)	8	8
Anneals	$10^4$	$10^4$
Regression window (window)	8 epochs	40 epochs
Regression stop (stop)	8 epochs	40 epochs

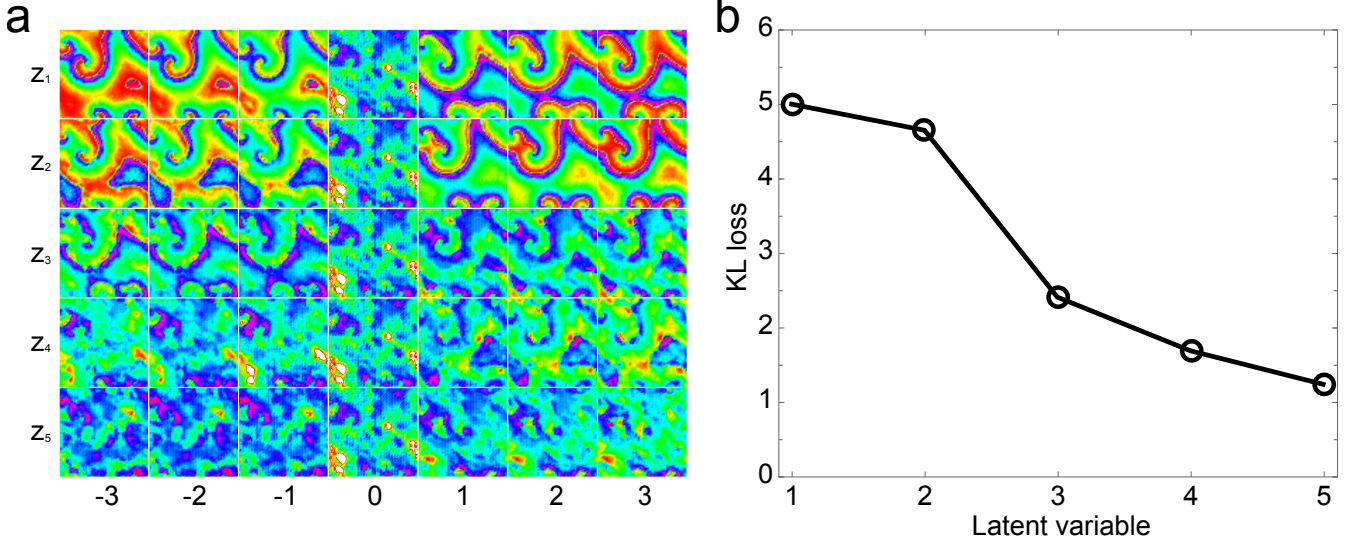


FIG. S1. Models trained on simulations of stable CGL dynamics often converge on two-dimensional models. Latent dimensions are numbered by KL loss. (a) Latent-dimension traversals change one variational-posterior mean while keeping others fixed at 0. Traversing latent dimensions  $z_1$  and  $z_2$  results in greater morphological change than traversing other latent dimensions. (b) KL loss between the aggregate-posterior marginal and a normal prior is markedly greater for  $z_1$  and  $z_2$  than for other latent dimensions, indicating that these dimensions encode more information.

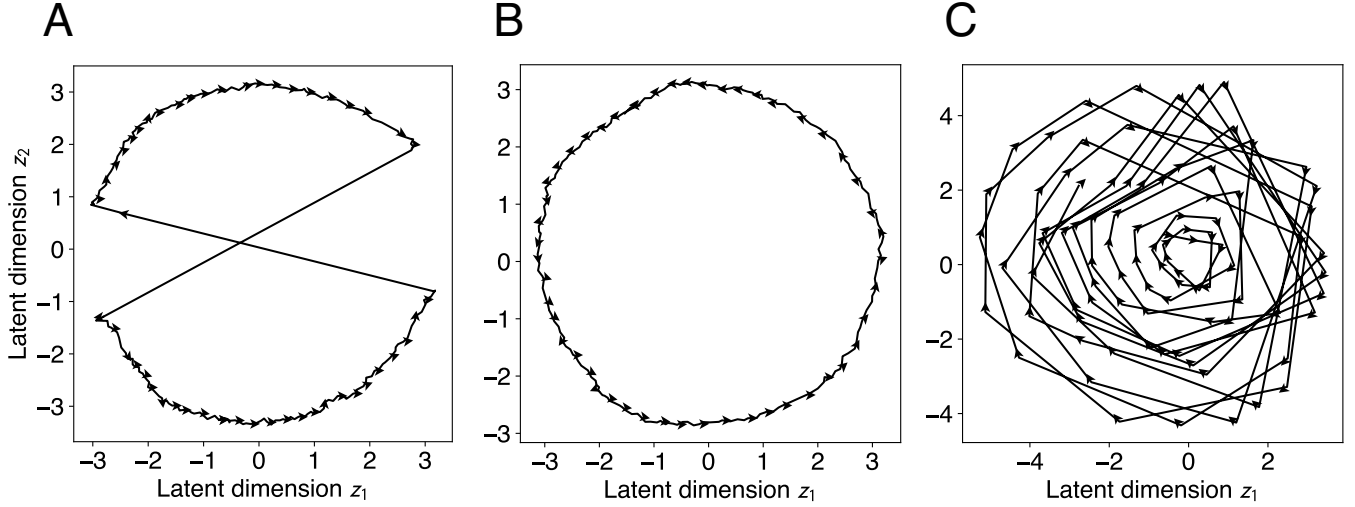


FIG. S2. Example latent trajectories. Arrows indicate forward temporal direction. (a) Discontinuous latent trajectory of a rejected model with training seed 1234 trained on a simulation dataset with  $c_1 = -1.0$ ,  $c_2 = 0.7$ , timestep 0.1, and initialization seed 16. (b) Continuous latent trajectory of an accepted model with training seed 1324 trained on the same simulation dataset as in (a). (c) Latent trajectory of a model with training seed 1234 trained on data from crop 1 of experiment  $i$ . Latent-trajectory continuity is difficult to establish visually in models of experiment datasets.

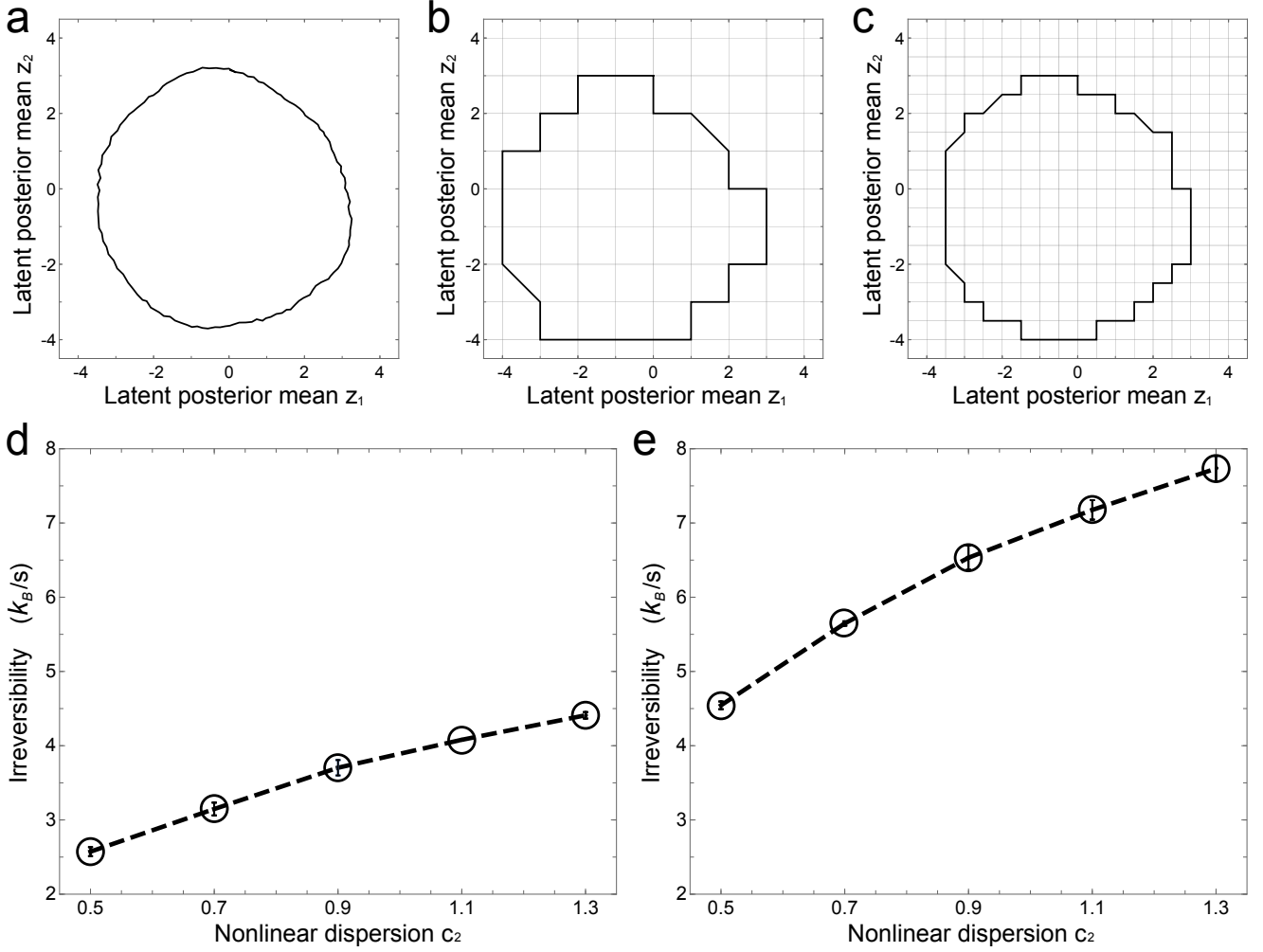


FIG. S3. Finer discretizations yield higher irreversibility estimates. Irreversibility estimates increase with nonlinear dispersion  $c_2$  and pattern complexity at fixed linear dispersion  $c_1$ . Irreversibility means and error bars denote averages and standard errors over three replicates. (a) The example latent trajectory from Fig. 2(d) (main text). (b) The trajectory in (a) discretized with  $b = 1$ . (c) The trajectory in (a) discretized with  $b = 0.5$ . (d) Estimated irreversibilities for the discretization shown in (b). (e) Estimated irreversibilities for the discretization shown in (c).

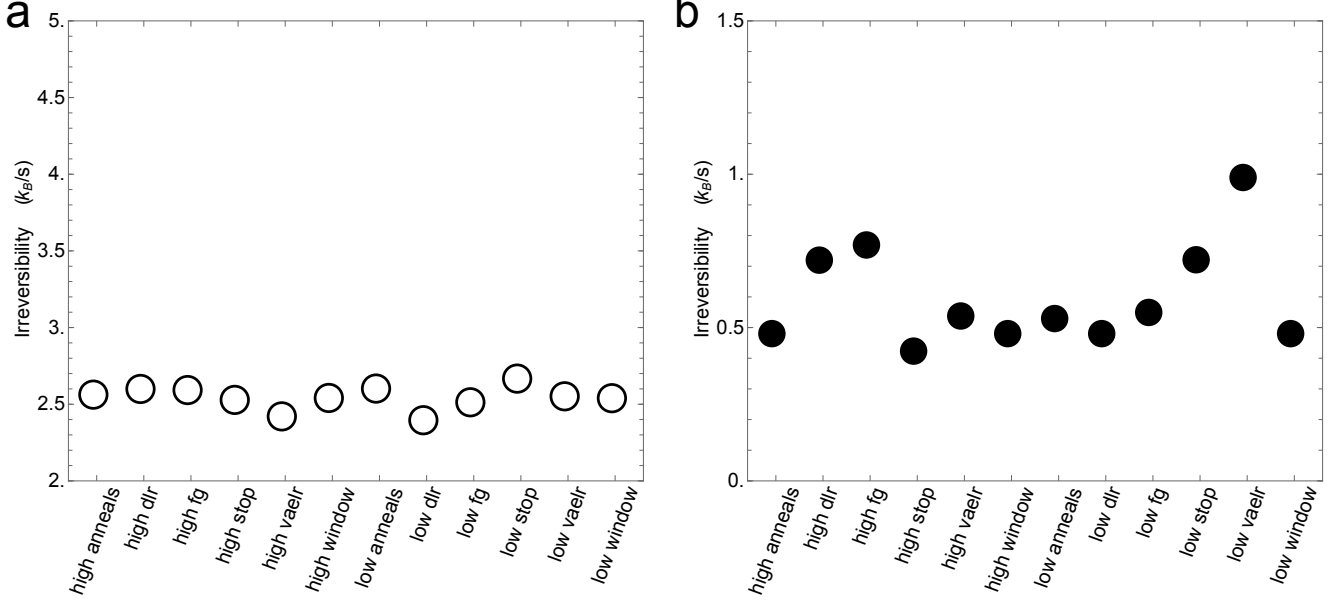


FIG. S4. Irreversibility estimates vary little with choice of hyperparameters. Points labeled “low” for each hyperparameter have the hyperparameter halved from its default value (Table S1), while points labeled “high” for each hyperparameter have the hyperparameter doubled from its default value. (a) Irreversibilities of models trained on a simulation dataset with  $c_1 = -0.2$ ,  $c_2 = 0.5$ , timestep 0.1, and initialization seed 0. (b) Irreversibilities of models trained on an experiment dataset from crop 1 of experiment  $i$ .

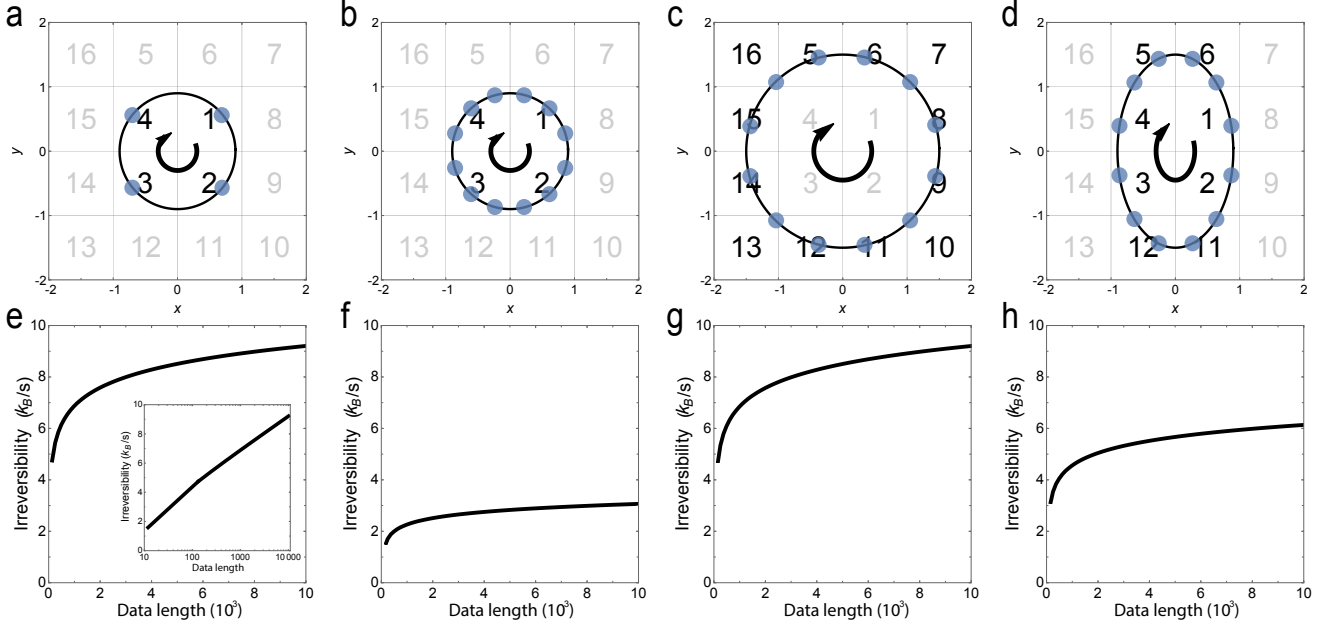


FIG. S5. Irreversibility estimates can be compared between deterministic trajectories. (a) Example cyclic trajectory. The arrow indicates direction and blue dots show points observed at a fixed sampling rate. Space is discretized into 16 bins of equal size. (b) The same dynamics as in (a) but evolving three times more slowly. (c) The same dynamics as in (b) but spatially dilated. (d) Example elliptical trajectory. (e) ZM irreversibility estimates calculated for the discretized series in (a) at different data lengths. Log-linear inset shows irreversibility increasing logarithmically with data length. (f) ZM irreversibility estimates calculated for the discretized series in (b) at different data lengths. (g) ZM irreversibility estimates calculated for the discretized series in (c) at different data lengths. (h) ZM irreversibility estimates calculated for the discretized series in (d) at different data lengths.

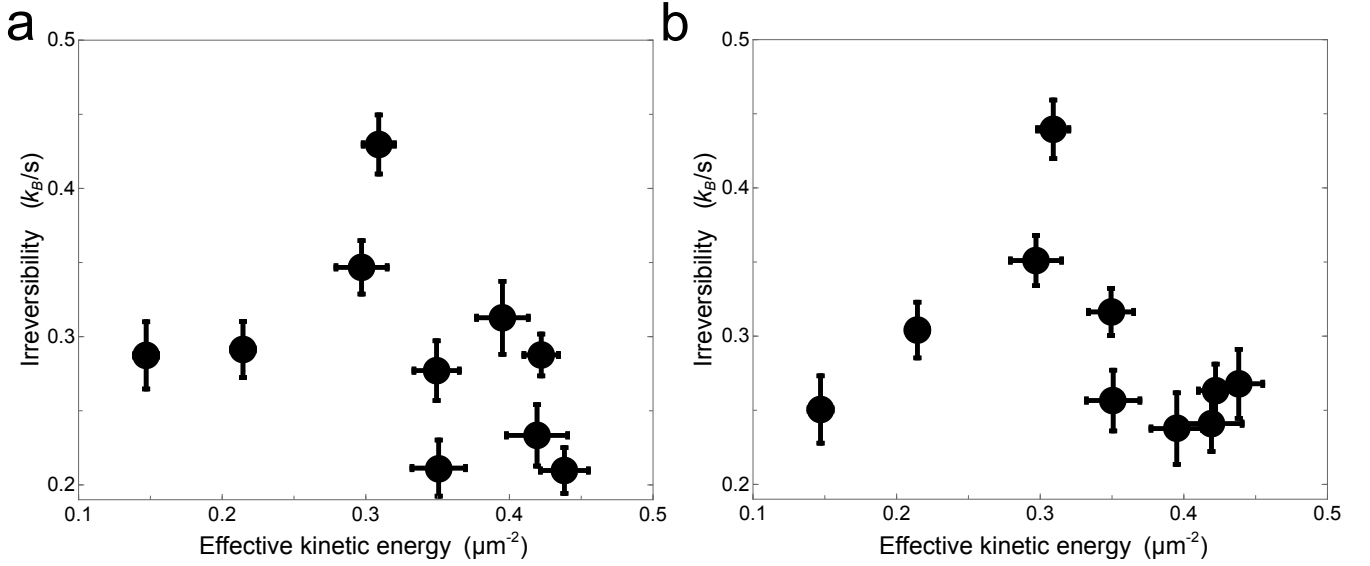


FIG. S6. Irreversibility estimates reflect experimental cell-activity levels. Effective kinetic energy is a measure of cell-activity level. As in Fig. 4(a), irreversibility estimates shown in each panel increase with cell-activity level in the stable regime (four points on the left) and are low in the turbulent regime (six points on the right). Irreversibility means and error bars denote averages and standard errors over training seeds; effective kinetic energy means and error bars denote averages and standard deviations over all pixels at all time points in the cell. (a) Crops shown in Fig. 4. (b) An additional crop of each experiment.

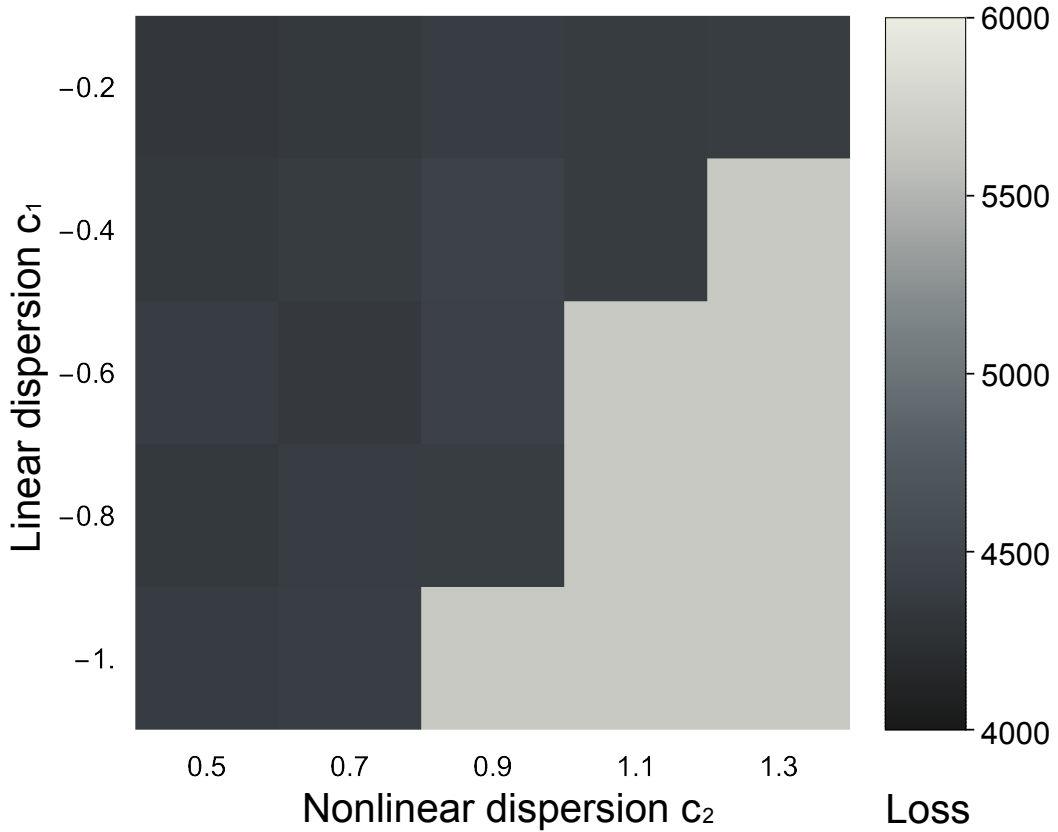


FIG. S7. FVAE reconstruction losses are higher for models trained on turbulent CGL dynamics than for models trained on stable CGL dynamics. Losses are averaged over models trained on three independent simulations. The trend is consistent with the observation that stable dynamics are better captured by latent representations than turbulent dynamics are.

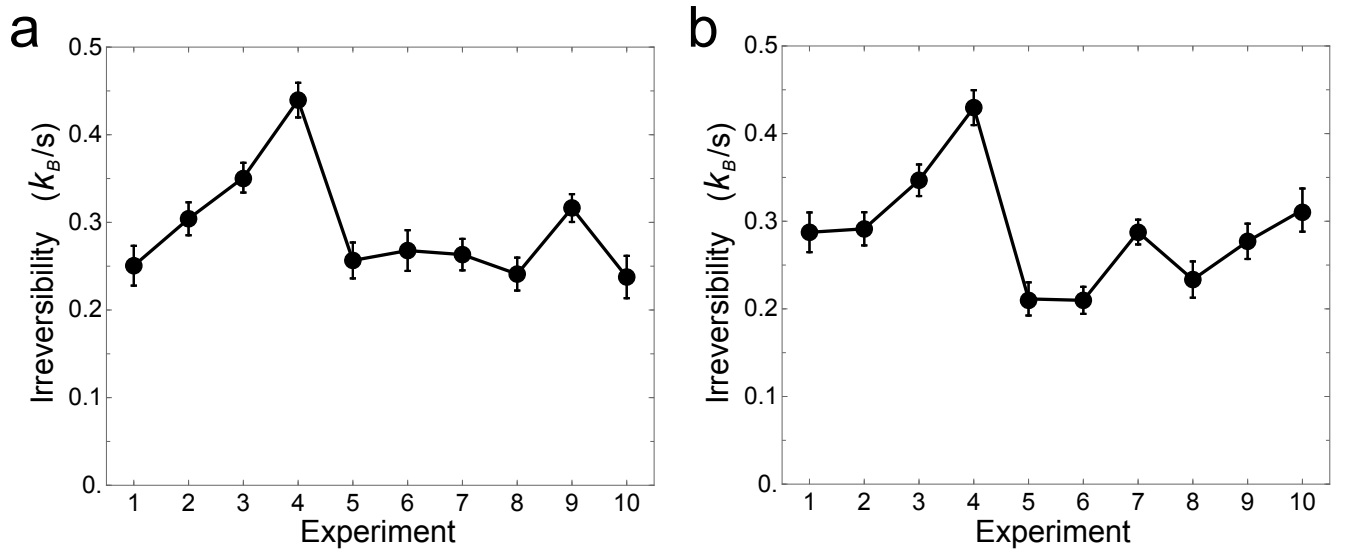


FIG. S8. Irreversibility estimate trends are robust to choice of experimental crop. Irreversibility estimates are shown for non-overlapping crops of each experiment shown in Fig. 4. Means and error bars denote averages and standard errors over training seeds. (a) Crops shown in Fig. 4. (b) An additional crop of each experiment.